Supporting Information

Two-dimensional materials as stabilized interphase for solid-state electrolyte $Li_{10}GeP_2S_{12}$ in lithium metal batteries

Jiachen Ma,[1] Ruge Quhe,[2,*] Zheyu Zhang,[1] Chen Yang,[1,3] Xiuying Zhang,[1] Jingzhen Li,[1] Lin Xu,[4] Jie Yang,[1] Bowen Shi,[1] Shiqi Liu,[1] Linqiang Xu,[1] Xiaotian Sun,[5] and Jing Lu[1,3,4,6,*]

[1] State Key Laboratory for Mesoscopic Physics and Department of Physics, Peking University, Beijing 100871, P. R. China.

[2] State Key Laboratory of Information Photonics and Optical Communications and School of Science, Beijing University of Posts and Telecommunications, Beijing 100876, P. R. China

[3] Academy for Advanced Interdisciplinary Studies, Peking University, Beijing 100871, P. R. China.

[4] Collaborative Innovation Center of Quantum Matter, Beijing 100871, P. R. China

[5] College of Chemistry and Chemical Engineering, and Henan Key Laboratory of Function-Oriented Porous Materials, Luoyang Normal University, Luoyang 471934, P. R. China

[6] Beijing Key Laboratory for Magnetoelectric Materials and Devices, Beijing 100871, P. R. China

[*] Corresponding author: quheruge@bupt.edu.cn (Ruge Quhe); jinglu@pku.edu.cn (Jing Lu)

1. The necessity of electronic insulation of the interphase layers

The interphase layer does not have to be electrically insulating but only conducts electrons in the direction of parallel to the interface (back and forth between the electrolyte and the electrode).

Though it used to be widely believed that the interface between the electrolyte and the electrodes should be electrically insulating to protect the electrolytes, some recent researches found that mixed ion-electron conductors can also be used as the interphase, as you said. We study these works very carefully and find that these battery systems using the mixed conducting interphase (MCI) have two characteristics in common: (1) The electrolyte and the electrode already have relatively good chemical and electrochemical stability (LiTFSI-DOL/DME electrolyte and Li metal anode[1], PEO electrolyte and Li metal anode[2], Ta-doped LLZO electrolyte+Li metal anode[3], and Ti-doped LLZO electrolyte+Li metal anode[4]); (2) The role of MCI is to conduct electrons parallel to the interface to guide a uniform electric field. In the works above, they still avoid those electron conductions perpendicular to the electrolyte and electrode interface. On the basis that SEI are electronic insulators, electronic conducting additives can be added inside or on one side of SEI.

Given that, we stress the application scope of the proposed two-dimensional interface screening method. For systems with poor electrolyte-electrode interface stability, the selection of interphases is suggested to ensure the electrochemical stability of the interface first. For systems with good electrolyte-electrode interface stability, mixed electronic-ionic interphases can be carefully designed to further inherit the dendrites growth and improve the performance of the battery.

2. Structural and electronic details of bulk LGPS

Table S1 Structural and electronic details of bulk LGPS: lattice constants, angles, band gaps under PBE and HSE06 functionals, respectively.

Lattice constants (Å)			Angles (°)			E_g (eV)	
a	*b*	*c*	*α*	*β*	*γ*	PBE	HSE06
8.747	8.747	12.869	89.994	89.998	90.471	2.28	3.37

3. Structural, electronic, and mechanical details of monolayer 2D materials

At the very beginning, 24 kinds of 2D SEI candidates are considered. Their structural, electronic, and mechanical parameters are listed in Table S2. Among them, 6 kinds of candidates have not been fabricated successfully but hold the phonon dispersion without imaginary frequency. For them, we calculate the exfoliation energies to judge their thermodynamic stability. *h*-BN is added for comparison. The exfoliation energies (E_{exf}) of the 2D materials are calculated as follows[5]

$$E_{exf} = \frac{E_{2D} - E_{bulk}}{A} \quad (1)$$

where E_{2D}, E_{bulk} refer to the total energy of isolated 2D materials and the corresponding most stable bulk structure with the same atom amount, respectively, and A refers to the in-plane area in the bulk structure. The most stable bulk structures of *h*-BN and *α*-BNyne are known[6, 7] To find the most stable bulk counterpart for the rest ones, different stacking types have been considered. The most stable bulk structures we found are framed by red squares, as shown in Fig. S1.

The calculated exfoliation energies of the seven materials are listed in Table S3. Marzari et al. obtain the exfoliation criterion through the statistical results of the exfoliation energy discrepancy in interlayer distances when calculated with the vdW and non-vdW functionals.[8] According to their criteria, the materials with exfoliation energies smaller than 30 meV/Å^2 are easily exfoliable, those with 30~130 meV/Å^2 exfoliation energies are potentially exfoliable, and those with exfoliation energies larger than 130 meV/Å^2 are difficult to exfoliate. Thus, among the seven materials, all the boron nitride compounds are easily exfoliable, and GeC is potentially exfoliable. In combination with the dynamical stability, these seven 2D materials have the potential to be SEI layers.

Table S2. Structural, electronic and mechanical details of three types (graphene-like, graphene nanomesh-like and graphyne-like from the top view) of monolyaer 2D materials: energy band gap (E_g) using LDA, GGA, HSE, GW approximations, respectively, inscribed circle diameter (d_i), in-plane stiffness (C), and available situations in experiment (Stable/Unstable represents its phonon dispersion hasn't/has imaginary frequency). The materials in each type are listed by band gaps (E_g) under GGA functional. The "~~strikeout~~" indicates that the index of this material does not meet the corresponding coarse sieve criteria.

Structure types	Materials	E_g (eV)						d_i (Å)	C (N/m)	Experiment available
		LDA	GGA	GGA this work	HSE	HSE this work	GW			
Graphene -like	*h*-BN	4.60[9]	4.69[10, 11], 4.56[12-14]	4.68	5.70[15], 5.56[12-14]	5.7	6.3-7.1[16], 7.4-8.4[12]	2.9[9], 2.51[11]	281[9], 271[17]	Yes[18]
	chair-graphane	3.385[19], 4.62[9]	3.7[20], 3.5[21], 3.477[19]	3.43	4.383[19]	4.38	6.05[20], 5.74[21]	2.6[22], 2.539[20]	246[9], 243[20]	Yes[23]
	chair-fluorographene	3.5[24]	3.2[20], 3.1[21, 25]	3.13	5.1[25], 4.933[19]	5.21	7.42[20], 7.4[21]	2.6[20]	232[9], 226[20]	Yes[22]
	AlN	3.08[26]	3.07[27], 2.91[15], 2.71[28]	2.78	4.04[15]	3.93	5.75[26]	3.09[26]	116[26]	Yes[29]
	SiC	2.52[26]	2.55[10], 2.53[30]	2.56	3.4[31], 3.35[15]	3.35	3.89[26]	3.07[26]	166[26]	Yes[32]
	GeC	2.09[26]	2.05[33]	2.05	2.87[15]	2.83	3.56[26]	3.22[26]	142[26]	Stable[26]
	GaN	2.27[26]	2.16[15], 1.96[27]	2.21	3.44[15], 3.23[34]	3.47	4.58[26]	3.20[26]	110[26, 34], 545.99 GPa[35]	Yes[29]
	2H-WS_2	1.98[36]	1.81[37], 1.64[27]	1.78	2.29[38], 1.93[39]	2.23	2.84[36]	3.13[36]	151[36]	Yes[36]
	2H-MoS_2	1.87[36]	1.8[10], 1.67[37], 1.59[27]	1.64	2.25[38], 1.88[39]	2.28	2.57[36]	3.11[36]	138[36]	Yes[36]
	GaP	1.92[26]	~~1.68~~[15]	-	2.65[15]	-	3.5[26]	3.84[26]	59[26]	Stable[26]
Graphene nanomesh -like	COF-1	-	3.50[40]	3.58	-	4.58	-	15.42[41]	41[40]	Yes[41]
	COF-5	-	2.25[40]	-	4.0[42]	-	-	30.02[41]	~~17~~[40]	Yes[41]
	C_2N	1.71[43]	1.77[44], 1.70[45], 1.66[46]	1.69	2.47[43]	2.47	3.75[43]	5.5[47]	71[47]	Yes[45, 48]
	g-C_3N_4	0.71[49]	~~1.19~~[49] ~~1.10~~[50]	-	2.70[51]	-	2.88[52]	4.76[53]	171~462[50]	Yes[54, 55]
	$MoCl_3$	-	~~0.8~~[10]	-	-	-	1.2[10]	3.2[56]	-	Yes[56]
	$MoBr_3$		~~0.56~~[10]	-	-	-	-	-	-	-
Graphyne -like	*γ*-BNyne	-	4.23[57], 4.21[11]	4.26	-	5.7	-	4.0[57]	-	Stable[57]
	6,6,12-BNyne	-	4.17[57]	4.25	-	5.68	-	4.8[57]	-	~~Unstable~~[57]
	α-BNyne	-	4.12[57]	4.15	-	5.55	-	7.1[57]	160 GPa[58]	Stable[57]
	β-BNyne	-	4.11[57]	4.14	-	5.54	-	7.2[57]	-	Stable[57]
	BNdiyne	-	3.85[11, 59]	3.92	-	5.32	-	5.0[59]	-	Stable[11]
	BNtriyne	-	3.81[11]	3.77	-	5.11	-	7.1[11]	-	Stable[11]
	graphdiyne	0.46[60]	~~0.53~~[61, 62]	-	1.10[61]	-	1.1[62, 63]	5.5[59]	123[64], 120[65]	Yes[65, 66]
	graphyne	0.52[67]	~~0.46~~[68]	-	0.96[68]	-	1.25[69]	4.0[68]	170 ~ 240[65], 166[64]	Yes[70, 71]

Table S3. Exfoliation energy of seven 2D materials.

Materials	E_{exf} (meV/Å^2)
h-BN	26.15
γ-BNyne	10.42
α-BNyne	14.96
β-BNyne	19.04
BNdiyne	13.45
BNtriyne	9.79
GeC	103.20

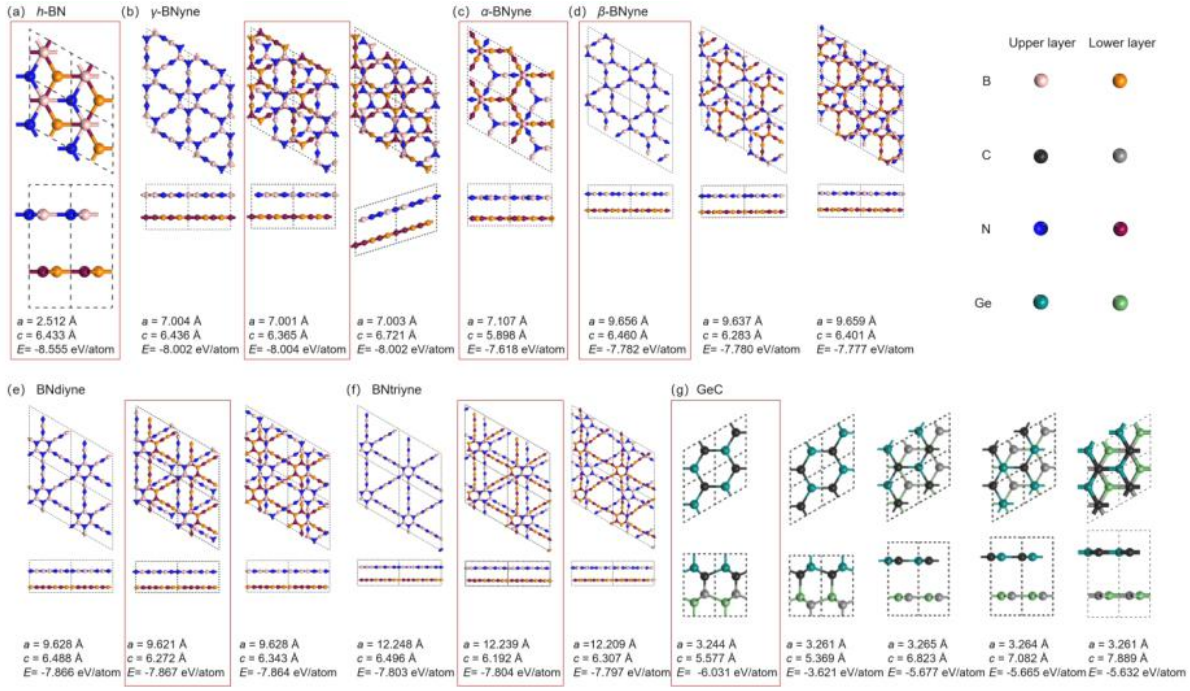

Figure S1. Structural diagrams of bulk (a) *h*-BN, (b) *γ*-BNyne, (c) *α*-BNyne, (d) *β*-BNyne, (e) BNdiyne, (f) BNtriyne, and (g) GeC. The corresponding lattice constant *a*, *c*, and energy per atom E are listed below. The structures framed by red squares are the most stable ones we find.

Then, we get 16 kinds of 2D materials that meet the above three requirements in the coarse sieve. They are ML *h*-BN, graphane, fluorographene, AlN, SiC, GeC, GaN, 2H-WS_2, 2H-MoS_2, COF-1, C_2N, *γ*-BNyne, *α*-BNyne, *β*-BNyne, BNdiyne, and BNtriyne, respectively. The initial structures are built in terms of the structural parameters reported in the literature. The structural diagrams are shown in Fig. S21, and the corresponding references are listed in Table S4. Geometry optimization is performed with common convergence thresholds of 10^{-3} eV Å^{-1} in force and 10^{-5} eV in energy.

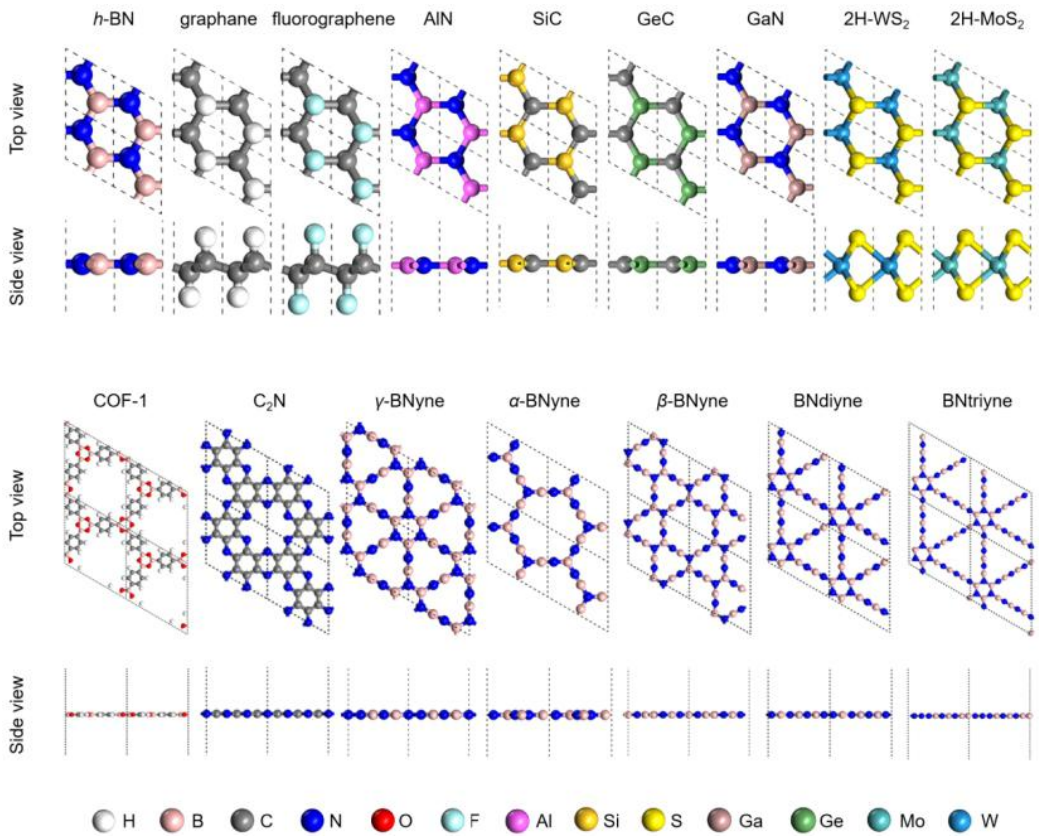

Figure S2. Top views and side views of *h*-BN, graphane, fluorographene, AlN, SiC, GeC, GaN, 2H-WS_2, 2H-MoS_2, COF-1, C_2N, *γ*-BNyne, *α*-BNyne, *β*-BNyne, BNdiyne, and BNtriyne monolayers.

Table S4. Lattice constants of 16 kinds of 2D materials and the corresponding references.

Materials	Lattice constant *a* (Å)	References
h-BN	2.510	Chem. Phys. Lett. 2018, 694, 102-106
graphane	2.539	Phys. Rev. B 2010, 82, (19), 195436
fluorographene	2.600	Phys. Rev. B 2010, 82, (19), 195436
AlN	3.168	Phys. Status Solidi B 2019, 256, (8), 1800759
SiC	3.096	Phys. Rev. B 2010, 81, (7), 075433
GeC	3.220	Phys. Rev. B 2009, 80, (15), 155453
GaN	3.200	Phys. Rev. B 2009, 80, (15), 155453
2H-WS_2	3.190f	Physica B Condens. Matter 2011, 406, (11), 2254-2260
2H-MoS_2	3.190	Physica B Condens. Matter 2011, 406, (11), 2254-2260
COF-1	15.020	Beilstein J. Nanotechnol. 2010, 1, 60-70
C_2N	8.330	Appl. Phys. Lett. 2015, 107, (23), 231904
γ-BNyne	7.010	Comput. Mater. Sci. 2017, 136, 12-19
α-BNyne	7.110	Comput. Mater. Sci. 2017, 136, 12-19
β-BNyne	9.660	Comput. Mater. Sci. 2017, 136, 12-19
BNdiyne	9.630	Chem. Phys. Lett. 2018, 694, 102-106
BNtriyne	12.260	Chem. Phys. Lett. 2018, 694, 102-106

There are 9 materials left after the fine sieve. In the graphene-like materials, there are *h*-BN, AlN, SiC, and GeC left. *h*-BN has much larger electrochemical windows than the rest, so *h*-BN is selected for the subsequent investigation. In the graphene nanomesh-like materials, no candidate meets the requirement. In the graphyne-like materials, there are *γ*-BNyne, *α*-BNyne, *β*-BNyne, BNdiyne, and BNtriyn left, and they have similar performance. To compare the five boron nitrogen compounds, the Atomistix ToolKit 2016 software package is adopted to gain the interface models. LGPS unit cell and three types of BNyne unit cells are used. In general, the strain and atom numbers are negatively correlated, and the time for calculating is proportional to the cubic number of atoms at least. Given that, the interface models are better to have less than 150 atoms and acceptable strains at the same time. The details for each interface with the most suitable atom numbers are listed in Table S5. With the similar numbers of atoms, LGPS/*γ*-BNyne and LGPS/BNtriyne have too large strains to calculate. LGPS/*α*-BNyne, LGPS/*β*-BNyne, and LGPS/BNdiyne hold small strains when they strain to both surfaces equally. Besides, *α*-BNyne is studied much more widely than *β*-BNyne and BNdiyne as far as we know. On the whole, we choose *α*-BNyne as 2D SEI as a representative of graphyne-like materials for further investigation. But in actual, *γ*-BNyne is also of the value of further research since the severe mismatch problem is not expected to appear in the experiment.

Table S5. Atom numbers and strains for LGPS/*γ*-BNyne, LGPS/*α*-BNyne, and LGPS/*β*-BNyne interfaces. *ε'* represents the maximum of ε_{11}, ε_{22}, and ε_{12}. *ε* represents the mean absolute strain.

interfaces	atoms	Strain 2D SEI's surface		Strain to both surfaces equally	
		ε'	*ε*	*ε*'	*ε*
LGPS/*γ*-BNyne	136	12.35	17.92	-8.17	5.74
LGPS/*α*-BNyne	132	-12.65	4.23	6.75	2.26
LGPS/*β*-BNyne	136	-9.46	4.69	-4.96	2.46
LGPS/BNdiyne	136	-9.17	4.83	4.81	2.47
LGPS/BNtriyne	124	-29.24	15.53	13.45	7.17

The structural diagrams of *h*-BN and *α*-BNyne are shown in Fig. S3 and their pores are marked in green. The lattice constants *a*, *b*, and inscribed circle diameter d_i are also marked in the diagram. We

can qualitatively divide *h*-BN into 2D materials with small-size pores and *α*-BNyne into those with large-size pores. For *h*-BN type 2D materials, the pristine pores are too small for Li-ions to flow through pores, then some point defects or line defects are needed. For *α*-BNyne type materials, the pristine pores are large enough for Li-ions to flow through directly.

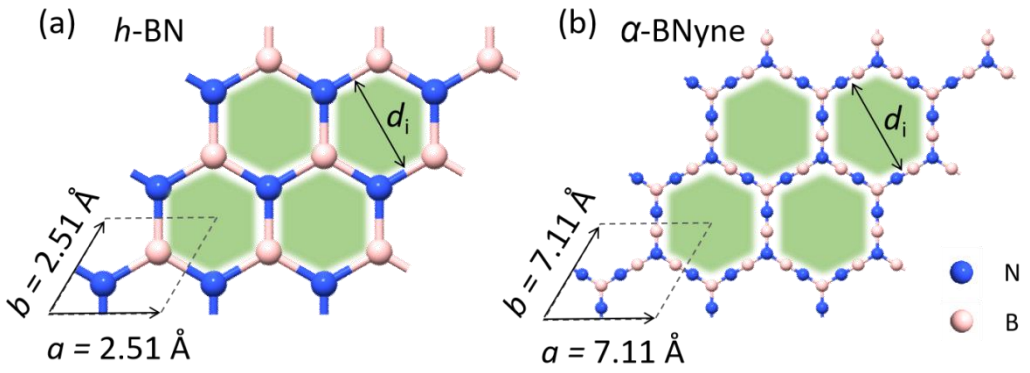

Figure S3. Top views of optimized ML (a) *h*-BN and (b) *α*-BNyne. The green shaded areas are the pores of the 2D sheets. The lattice constants (*a* and *b*) and inscribed circle diameter (d_i) are marked in the diagram.

4. The electrochemical window

The electrochemical window is the electrochemical potential range where the electrolyte will neither be reduced nor oxidized, with the lower limit being the reduction potential and the upper limit being the oxidation potential in the voltage scale. The cell can be electrochemically stable only when the electrochemical potential (their Fermi potential) of the anode and cathode are both within the electrochemical window. It takes the Fermi potential of metallic lithium in lithium metal battery (LMB) as the zero baseline. Taking $Li_{10}GeP_2S_{12}$ (LGPS) as an example, its electrochemical window is 1.71-2.14 V, which means that the reduction potential is 1.71 V, and the oxidation potential is 2.14 V. Since its reduction potential is higher than the Fermi potential of metallic lithium, LGPS is unstable against the lithium metal anode. On the electronic energy scale, the upside-down relationships need to be inverted. It corresponds to the reduction energy level of LGPS being 1.71 eV lower than the Fermi level of lithium metal. The schematic diagram of the electrochemical windows under the potential scale and the energy scale are depicted in Fig. S4.

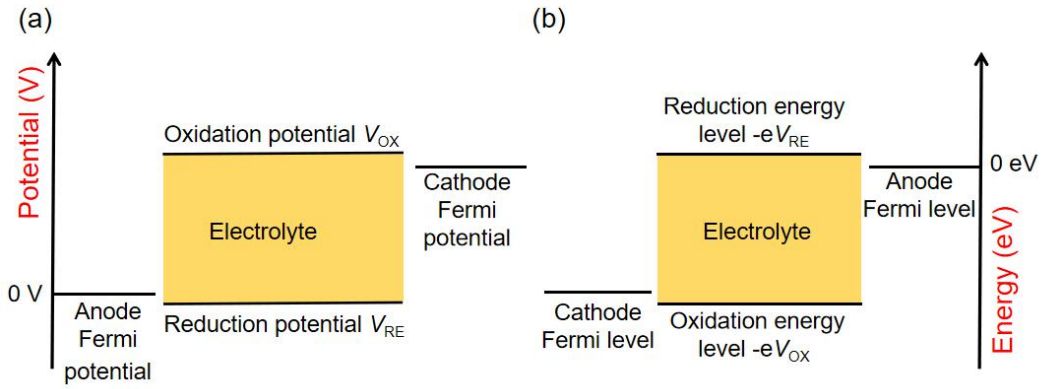

Figure S4. Schematic diagram about the electrochemical window under (a) the potential scale and (b) the energy scale. The upside-down relationship between the two is inverted.

5. The interface modeling

The surface energy $E_{surface}$ is defined as follows to determine the thermodynamic stability of slab models

$$E_{surface} = \frac{1}{2A}(E_{slab} - E_{bulk})$$

where E_{bulk}, E_{slab}, and A refer to the total energy of bulk LGPS unit cell, LGPS slab unit cell, and the sectional area, respectively. The LGPS slabs are obtained by adding vacuum space to bulk LGPS unit cell in the c direction. One bulk LGPS has six layers of inequitable PS_4- or GeS_4- tetrahedron. According to the structural feature, there are six possible slabs terminated with PS_4 or GeS_4 tetrahedron, as shown in Fig. S5.

The surface energies of these six slabs are listed in Table S3. The lower of $E_{surface}$, the more stable of the surface. The s6-PS_4 terminated slab has the lowest surface energy. Thus, the LGPS/Li, LGPS/*h*-BN/Li, and LGPS/*α*-BNyne/Li interface structures are all constructed with s6-PS_4 terminated slab. The structural and electronic details of the LGPS/(2D SEI)/Li Interfaces are listed in Table S6.

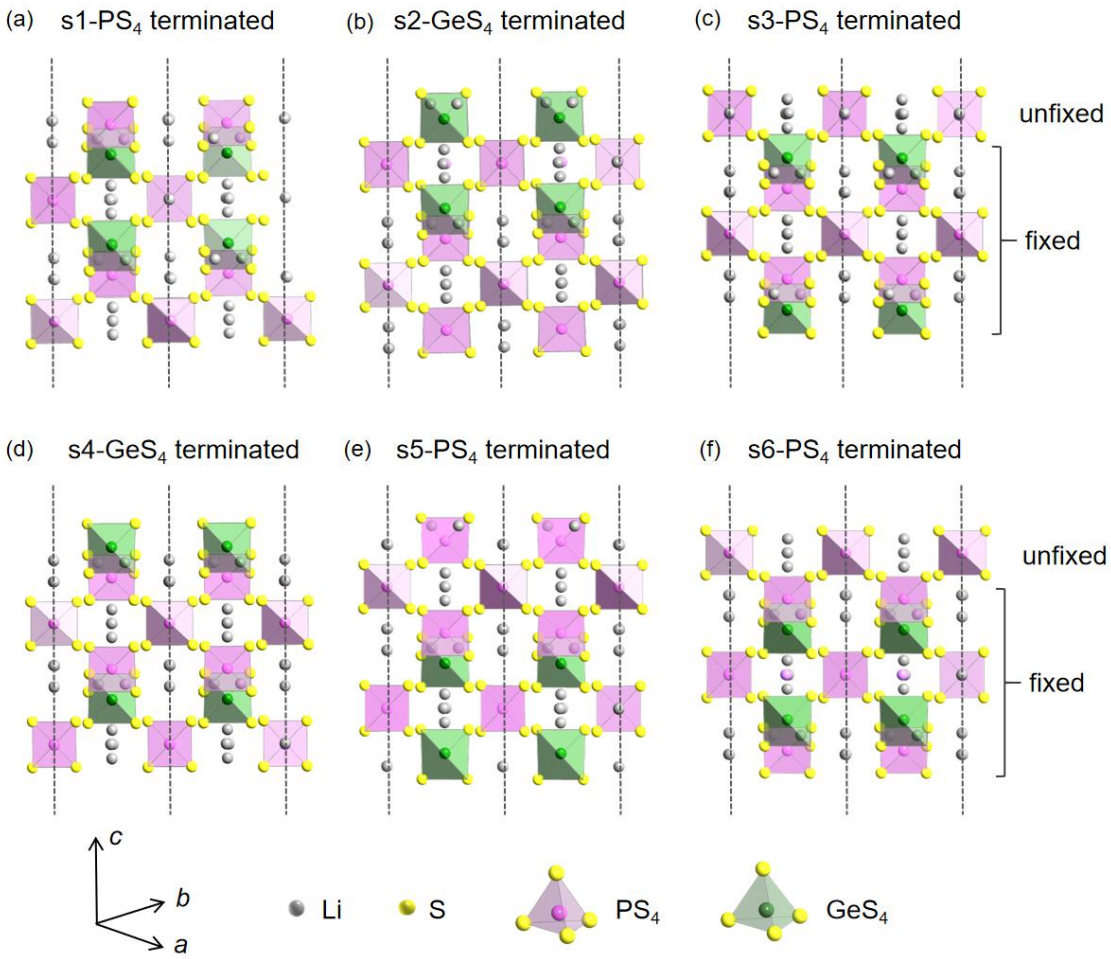

Figure S5. Six possible slabs with PS_4 or GeS_4 tetrahedron terminated, marked from s1 to s6. The bottom five layers of tetrahedrons are fixed uniformly, while the surface tetrahedron-layer is unfixed and relaxed.

Table S6. The surface energies ($E_{surface}$) of six possible PS_4 and GeS_4-terminated structures.

Structures	$E_{surface}$ (eV/Å^2)
s1-PS_4 terminated	0.026
s2-GeS_4 terminated	0.052
s3-PS_4 terminated	0.044
s4-GeS_4 terminated	0.048
s5-PS_4 terminated	0.048
s6-PS_4 terminated	0.025

Table S7. Structural and electronic details of the LGPS/Li, LGPS/*h*-BN/Li and LGPS/*α*-BNyne/Li interface structures: lattice mismatches (ε) of the LGPS slab/ML 2D materials interfaces (LGPS-2D) and the ML 2D materials/Li metal interfaces (2D-Li), respectively, vertical distances (h) of the LGPS-2D and 2D-Li interfaces, respectively, formation energies (E_{form}), and Li diffusion barriers along the interfaces (ΔE_{al}) as well as across the interfaces (ΔE_{ac}). The LGPS/*h*-BN/Li structure has a pair of B-N vacancies in the barrier calculation across the interface.

Structures	ε (Å)		h (Å)		E_{form}	Li diffusion barriers	
	LGPS-2D	2D-Li	LGPS-2D	2D-Li	(eV/atom)	ΔE_{al}	ΔE_{ac}
LGPS/Li	1.31%		-	-	0.0627	0.23	0.26
LGPS/*h*-BN/Li	2.70%	1.31%	2.40	2.28	0.0136	0.28	0.29
LGPS/*α*-BNyne/Li	2.26%	1.22%	2.85	2.79	-0.0047	0.09	0.15

6. Hybrid states in LGPS/Li interface

To make the "hybrid states" more clear, we project the density of states to each orbital of the elements involved. Since the hybrid states appear in L2 and L3 in LGPS/Li interface, we focus on these two layers. As shown in Fig. R6, the hybrid states in L2 are mainly contributed by p orbital of S element, and that in L3 are jointly contributed by p orbital of P element and p orbital of S element. These hybrid states confirm that LGPS and lithium metal will react to form unstable interfaces.

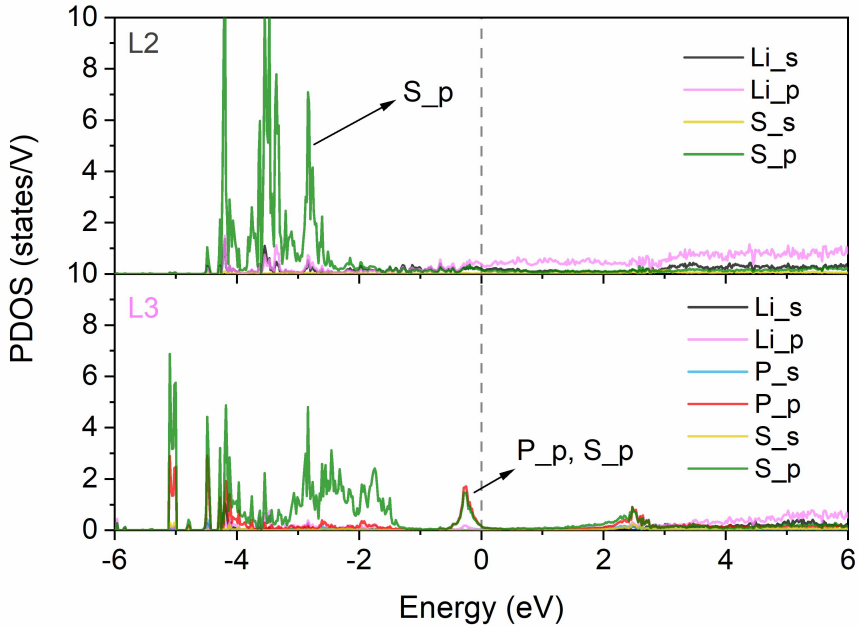

Figure S6. PDOS of L2 and L3 in LGPS/Li structure. The hybrid states in L2 are mainly contributed by p orbital of S element, and that in L3 are jointly contributed by p orbital of P element and p orbital of S element.

7. Energy barriers in the LGPS/2D SEI/Li interfaces

(1) The low energy barrier when along the LGPS/α-BNyne/Li interface

The low energy barrier is found along the LGPS/α-BNyne/Li interface and it is speculated to be related to the structure of α-BNyne and the environment of the interface.

In Fig. S7(a), the intrinsic α-BNyne has relatively large lattice constants of $a = b$ =7.11 Å and a large pore. The total energy of the Li adsorbed α-BNyne is hardly changed when the Li atom is located close to the center of the pore. This implies that the diffusion of the Li atom near the pore center is less affected by α-BNyne. We further performed the climbing-image nudged elastic band (CI-NEB) calculation. As shown in Fig. S7(b), the energy barrier of the Li atom migrating in the pore of the α-BNyne monolayer is 0.34 eV, which is also consistent with the variation of the total energy according to the energy map.

Besides, the environment of the interface may lessen the energy barrier further. In terms of the Bader charge analysis, we found that the charges of the Li metal around the migration path change greatly while those in α-BNyne and LGPS barely change during the Li migration. It can be speculated that the Li metal helps the migration of the Li atom along the interface by redistributing the valence charge.

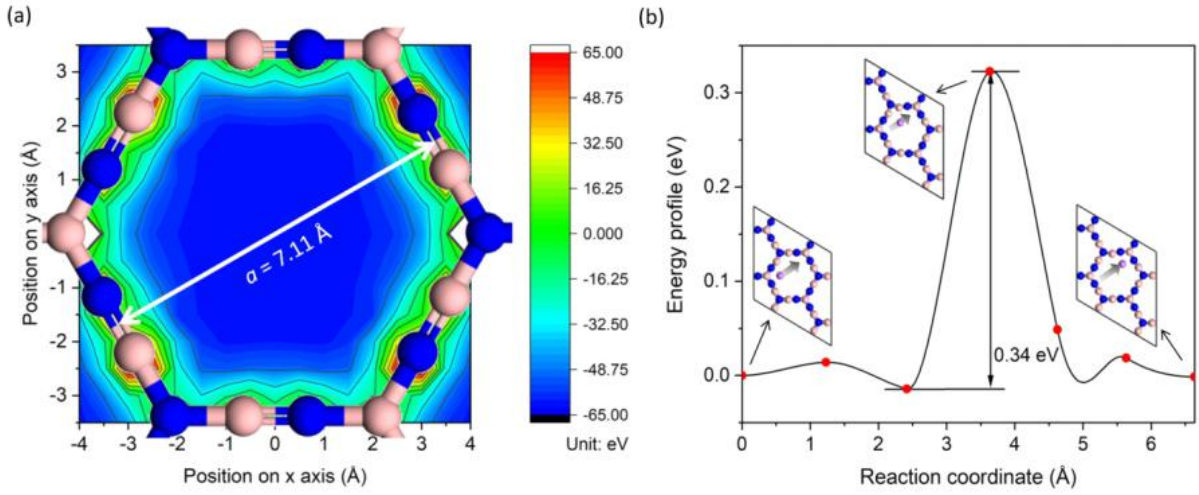

Figure S7. (a) Energy map the intrinsic α-BNyne monolayer with its top views. (b) Energy profile of one Li atom migrating in the pore of the α-BNyne monolayer. The blue, nude, and purple spheres represent N, B, and Li atoms, respectively.

(2) The barrier difference when across the LGPS/*h*-BN(BNV)/Li interface

The diffusion barrier of Li on the free-standing *h*-BN layers with vacancies (h-BN(BNV)) is 0.92 eV, as reported in the previous literature[72]. The diffusion barriers according to our CI-NEB calculations are 0.29 and 0.76 eV when the Li atom migrates from LGPS side to *h*-BN(BNV) and the Li metal side to *h*-BN(BNV), respectively. The barriers in the interface are smaller than those in literature. It is speculated that the barrier difference is the result of the interfacial environment, and the difference between LGPS and the Li metal results in the barrier variation under the two directions. To further investigate the influence of the interfacial environment, the bond lengths and Bader charge of the free-standing *h*-BN(BNV) and *h*-BN(BNV) between Li metal and LGPS are listed in Table S8. The initial states and transition states are chosen for comparison. Compared with those in the free-standing *h*-BN(BNV), the changes of the bond lengths of the migrating Li atom and its surrounding B, N atom, and the changes of their Bader charge from the initial state to the transition state are both smaller in the interface. Therefore, the change of the Coulomb attraction of the *h*-BN layer to the Li-ion is smoother in the interface, and thus the energy barrier is smaller.

Table S8. Bond lengths (*L*) and Bader charge (*Q*) with the migrating Li atom in the free-standing *h*-BN(BNV) and the LGPS/*h*-BN(BNV)/Li interface. Subscripts i and t represent the initial and transition states, respectively.

Atoms	Free-standing *h*-BN		*h*-BN in the interface	
	L_t-L_i (Å)	Q_t-Q_i (e)	L_t-L_i (Å)	Q_t-Q_i (e)
Li	-	0.042	-	0.039
B1	0.040	-0.025	-0.070	-0.025
B2	-0.074	-0.049	-0.224	-0.011
B3	-0.171	0.001	-0.026	-0.002
B4	-0.447	0.044	-0.325	0.000
B5	-0.331	-0.017	-0.225	0.008
B6	-0.222	-0.005	-0.163	0.003
B7	-0.150	-0.013	-0.088	-0.013
N1	-0.207	0.044	-0.237	0.024
N2	0.106	-0.011	-0.123	-0.017
N3	0.023	-0.001	-0.054	-0.010
N4	-0.409	-0.010	-0.149	0.006
N5	-0.509	0.000	-0.367	0.025
N6	-0.067	0.079	-0.090	-0.001
N7	-0.216	-0.036	-0.109	0.016
Total	-2.634	0.044	-2.250	0.043

(3) The large energy barriers when away from the interfaces

The enlarged diffusion barriers are believed as the result of the longer path, which reflects a more comprehensive migration situation. When the Li atom moves deeply into LGPS or the Li metal, the energy becomes high due to the limitation of the applied slab model in which the atoms away from the interfaces are fixed and cannot flow out when the selected Li atom squeeze in.

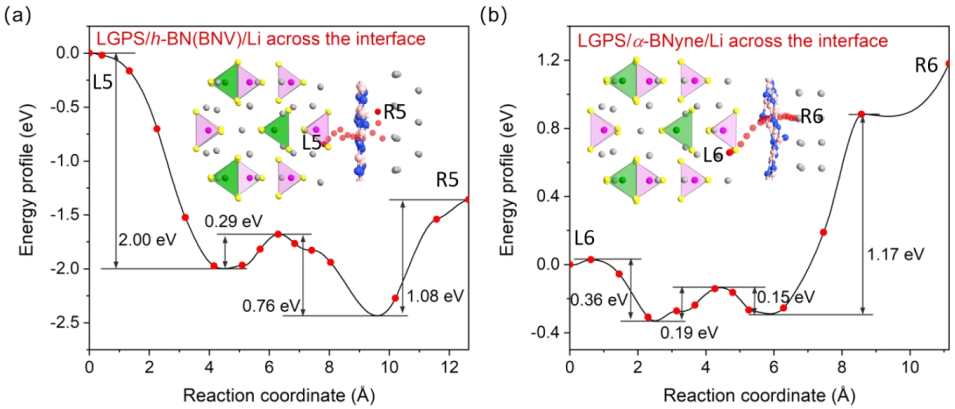

Figure S8. Energy profiles of Li-ion moving across the interface of the (a) LGPS/*h*-BN(BNV)/Li and (b) LGPS/*α*-BNyne/Li systems. The gray, green, pink, yellow, nude, and blue spheres represent Li, Ge, P, S, B, and N atoms, respectively. In each illustration, the red spheres mark the migration path of the selected Li-ion, and each of them corresponds to an image, both from the left (LGPS) to the right (the Li metal).

8. Barriers with multiple 2D sheets

With the increase of the layer number of 2D sheets in the interface, the internal environment becomes closer to the pristine multiple 2D sheets. And also limited by the computational power, we simulate the Li-ion migration in the slabs with multiple 2D sheets and compare the influence of the number of 2D sheets.

A slab with 4 layers of AB-stacked *h*-BN is constructed, and two pores that do not wholly overlap each other from the top view are set in the two inner layers of *h*-BN, just to make the situation more general. As shown in Fig. S9(a), there is a negligible energy barrier when Li-ion moves close to the first pore. Then, the energy drops by 0.24 eV when the Li-ion passes through the first pore and then rises by 0.30 eV when it passes through the second pore, indicating that the energy is much lower when the Li-ion is sandwiched between two pores. Based on the initial structural energy, the Li-ion

migrating through two layers of *h*-BN holds an energy barrier of 0.06 eV and an energy well of 0.24 eV. The energy barrier is even much smaller than the energy barrier (0.38 eV) for the Li-ion migrating through the *h*-BN monolayer with the same pore. It is worth noting that when the Li-ion migrates between multiple *h*-BN layers, *h*-BN layers shift. To further investigate the local situation between the two pores, the total energies of the unshifted *h*-BN slab (Image 1) and shifted *h*-BN slab (Image 4) with a Li-ion adsorbed on different locations are further calculated, respectively. According to the energy maps in Fig. S9(c), the energy is lower when the Li-ion is closer to the center of the pore. Compared with the unshifted *h*-BN slab, the shifted one has a more even energy distribution, which is likely to reduce the energy barrier.

A similar analysis is carried out for the slab with 4 layers of AB-stacked *α*-BNyne. As shown in Fig. S10(a), the two energy peaks (Image 3 and 7) appear when the Li-ion is in the *α*-BNyne layer during the whole migrating process. The Li-ion is closer to the BN chain in Image 3 and is closer to the center of the hexagonal pore in Image 7, which can explain the energy difference between these two images. Between the two peaks, there is an energy valley of Image 6. Based on the initial structural energy, the energy barriers of the Li-ion migrating through the first pore and the second pore are 0.41 and 0.06 eV, respectively. By contrast, when the Li-ion passes through the *α*-BNyne monolayer from the center of the intrinsic hexagonal pore, there is an energy well of 0.12 eV, rather than an energy barrier; that is, the Li-ion prefers to stay in the plane of the *α*-BNyne monolayer. As shown in Fig. S10(c), the energy is low when the Li-ion close to the center of the pores, and there is a rhombic overlap of the low energy area from the top view. In the *α*-BNyne slab, the Li-ion migrates through the low energy channel (around x = 5 Å, y = 1.5 Å), and no obvious shift occurs in the *α*-BNyne slab. Thus, the Li-ion migrating paths and barriers depend on the specific local situation of the *α*-BNyne sheets.

To conclude, according to the first-principles calculations, the shifts of *h*-BN layers decrease the energy barrier. And the migration barrier in the *α*-BNyne slab varies, depending on the specific environment.

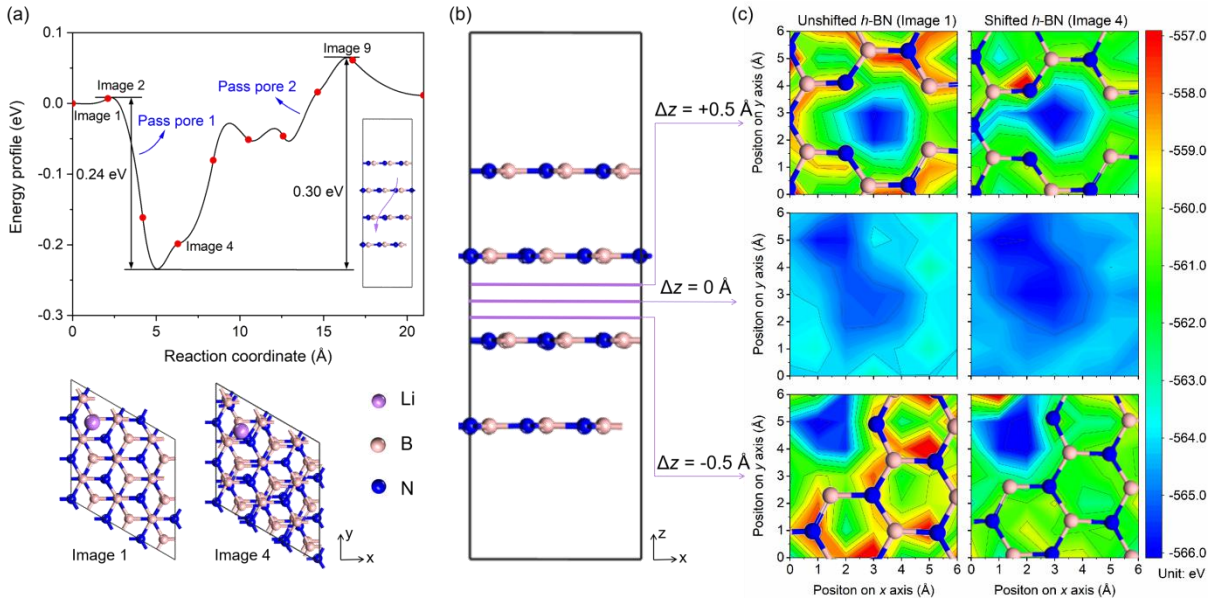

Figure S9. (a) Energy profiles of the Li-ion migrating through the two inner pored *h*-BN layers the slab with 4 layers of *h*-BN with top views of Image 1 and 4. Two pores that do not wholly overlap each other from the top view are set in the two inner layers of *h*-BN. (b) Side view of *h*-BN layers and (c) its energy maps when one Li-ion is placed between the two inner layers in the unshifted *h*-BN slab (*h*-BN in Image 1) and shifted *h*-BN slab (*h*-BN in Image 4), respectively. Δ*z* is defined as the difference of the vertical distance between the Li-ion and the middle point of the two inter *h*-BN layers.

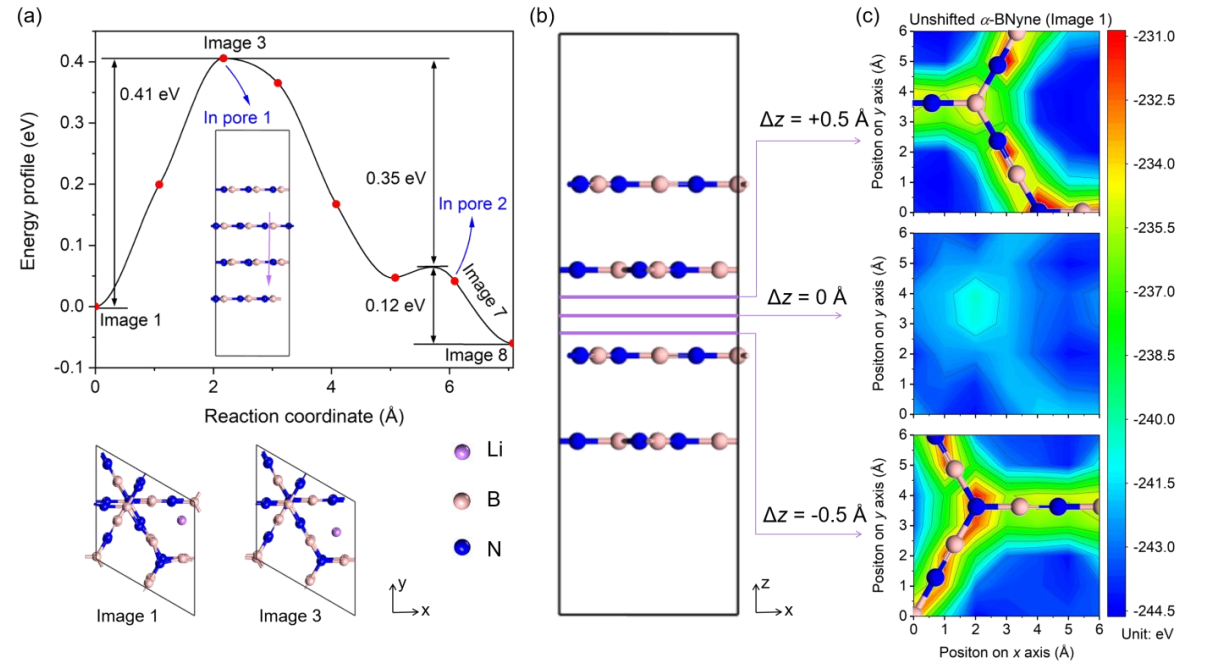

Figure S10. (a) Energy profiles of the Li-ion migrating through the two inner *α*-BNyne layers the slab with 4 layers of *α*-BNyne with top views of Image 1 and 3. (b) Side view of *α*-BNyne layers and (c) its energy maps when one Li-ion is placed between the two inner layers in the unshifted *α*-BNyne slab (*α*-BNyne in Image 1). Δ*z* is defined as the difference of the vertical distance between the Li-ion and the middle point of the two inter *α*-BNyne layers.

9. The kinetics of electron and Li-ion transport *vs.* thermodynamics

The relationship between the kinetics and thermodynamics of electron and Li-ion transport is very complicated.

According to the Hammond-Leffler rule, the smaller the energy difference between the reactants and the products, the smaller the reaction activation energy and the faster carrier transport in general. And the thermodynamics of electron and Li-ion transport can be measured by the Gibbs free energy of the reactants and the products based on density functional theory (DFT).

The kinetics of electron transport can be calculated by the nonequilibrium Green's function (NEGF) combined with DFT. An electric field can be applied to the interface between the semi-infinite electrolyte and the semi-infinite electrode. The calculated transmission spectra and scattering states could provide key information of the electron transport under bias. However, the relationship between thermodynamics and kinetics in batteries is rather complicated and needs a lot of computations. Though such kind of simulation is time-consuming considering the large model and limited computing power, it might be feasible in the near future when the computational capacity improves.

The kinetics of Li-ions can be calculated by *ab initio* molecular dynamics (AIMD) simulation. However, a decent model of the interested system (Li metal/2D materials/LGPS interfaces) are estimated to include a few thousand atoms. Performing such AIMD simulation in the macroscopic time scale remains challenging due to the current limited computational power.

Though we didn't investigate much here, the thermodynamics and kinetics of the electron and ion transport is an interesting and challenging topic. We encourage readers of this article to propose feasible methods to study it in detail.

References

(1) C. Yan, X.-B. Cheng, Y.-X. Yao, X. Shen, B.-Q. Li, W.-J. Li, R. Zhang, J.-Q. Huang, H. Li and Q. Zhang, An Armored Mixed Conductor Interphase on a Dendrite-Free Lithium-Metal Anode. *Adv. Mater.* **2018,** 30, (45), 1804461.

(2) M. Yan, J.-Y. Liang, T.-T. Zuo, Y.-X. Yin, S. Xin, S.-J. Tan, Y.-G. Guo and L.-J. Wan, Stabilizing Polymer–Lithium Interface in a Rechargeable Solid Battery. *Adv. Funct. Mater.* **2020,** 30, (6), 1908047.

(3) H. Huo, Y. Chen, R. Li, N. Zhao, J. Luo, J. G. Pereira da Silva, R. Mücke, P. Kaghazchi, X. Guo and X. Sun, Design of A Mixed Conductive Garnet/Li Interface for Dendrite-Free Solid Lithium Metal Batteries. *Energy Environ. Sci.* **2020,** 13, (1), 127-134.

(4) J. Gao, J. Zhu, X. Li, J. Li, X. Guo, H. Li and W. Zhou, Rational Design of Mixed Electronic-Ionic Conducting Ti-Doping $Li_7La_3Zr_2O_{12}$ for Lithium Dendrites Suppression. *Adv. Funct. Mater.* **2020,** n/a, (n/a), 2001918.

(5) J. H. Jung, C.-H. Park and J. Ihm, A Rigorous Method of Calculating Exfoliation Energies from First Principles. *Nano Lett.* **2018,** 18, (5), 2759-2765.

(6) P. Jiang, X. Qian, R. Yang and L. Lindsay, Anisotropic Thermal Transport in Bulk Hexagonal Boron Nitride. *Phys. Rev. Mater.* **2018,** 2, (6), 064005.

(7) S. Behzad, Structural and Electro-Optical Properties of Bilayer Graphyne Like BN Sheet. *Solid State Commun.* **2016,** 248, 27-31.

(8) N. Mounet, M. Gibertini, P. Schwaller, D. Campi, A. Merkys, A. Marrazzo, T. Sohier, I. E. Castelli, A. Cepellotti, G. Pizzi and N. Marzari, Two-Dimensional Materials from High-Throughput Computational Exfoliation of Experimentally Known Compounds. *Nat. Nanotechnol.* **2018,** 13, (3), 246-252.

(9) A. Bhattacharya, S. Bhattacharya and G. P. Das, Strain-Induced Band-Gap Deformation of H/F Passivated Graphene and *h*-BN Sheet. *Phys. Rev. B* **2011,** 84, (7), 075454.

(10) P. Miró, M. Audiffred and T. Heine, An Atlas of Two-Dimensional Materials. *Chem. Soc. Rev.* **2014,** 43, (18), 6537-6554.

(11) X.-D. Li and X.-L. Cheng, Predicting the Structural and Electronic Properties of Two-Dimensional Single Layer Boron Nitride Sheets. *Chem. Phys. Lett.* **2018,** 694, 102-106.

(12) N. Berseneva, A. Gulans, A. V. Krasheninnikov and R. M. Nieminen, Electronic Structure of Boron Nitride Sheets Doped with Carbon from First-Principles Calculations. *Phys. Rev. B* **2013,** 87, (3), 035404.

(13) N. Berseneva, A. V. Krasheninnikov and R. M. Nieminen, Mechanisms of Postsynthesis Doping of Boron Nitride Nanostructures with Carbon from First-Principles Simulations. *Phys. Rev. Lett.* **2011,** 107, (3), 035501.

(14) B. Huang and H. Lee, Defect and Impurity Properties of Hexagonal Boron Nitride: A First-Principles Calculation. *Phys. Rev. B* **2012,** 86, (24), 245406.

(15) I. Guilhon, D. S. Koda, L. G. Ferreira, M. Marques and L. K. Teles, Approximate Quasiparticle Correction for Calculations of the Energy Gap in Two-dimensional Materials. *Phys. Rev. B* **2018,** 97, (4), 045426.

(16) F. Hüser, T. Olsen and K. S. Thygesen, Quasiparticle GW Calculations for Solids, Molecules, and Two-Dimensional Materials. *Phys. Rev. B* **2013,** 87, (23), 235132.

(17) D. Akinwande, C. J. Brennan, J. S. Bunch, P. Egberts, J. R. Felts, H. Gao, R. Huang, J.-S. Kim, T. Li, Y. Li, K. M. Liechti, N. Lu, H. S. Park, E. J. Reed, P. Wang, B. I. Yakobson, T. Zhang, Y.-W. Zhang, Y. Zhou and Y. Zhu, A Review on Mechanics and Mechanical Properties of 2D Materials—Graphene and Beyond. *Extreme Mech. Lett.* **2017,** 13, 42-77.

(18) L. Song, L. Ci, H. Lu, P. B. Sorokin, C. Jin, J. Ni, A. G. Kvashnin, D. G. Kvashnin, J. Lou, B. I. Yakobson and P. M. Ajayan, Large Scale Growth and Characterization of Atomic Hexagonal Boron Nitride Layers. *Nano Lett.* **2010,** 10, (8), 3209-3215.
(19) M. N. Amini, O. Leenaerts, B. Partoens and D. Lamoen, Graphane- and Fluorographene-Based Quantum Dots. *J. Phys. Chem. C* **2013,** 117, (31), 16242-16247.
(20) O. Leenaerts, H. Peelaers, A. D. Hernández-Nieves, B. Partoens and F. M. Peeters, First-principles Investigation of Graphene Fluoride and Graphane. *Phys. Rev. B* **2010,** 82, (19), 195436.
(21) M. Klintenberg, S. Lebègue, M. I. Katsnelson and O. Eriksson, Theoretical Analysis of the Chemical Bonding and Electronic Structure of Graphene Interacting with Group IA and Group VIIA Elements. *Phys. Rev. B* **2010,** 81, (8), 085433.
(22) M. Inagaki and F. Kang, Graphene Derivatives: Graphane, Fluorographene, Graphene Oxide, Graphyne and Graphdiyne. *J. Mater. Chem. A* **2014,** 2, (33), 13193-13206.
(23) D. C. Elias, R. R. Nair, T. M. G. Mohiuddin, S. V. Morozov, P. Blake, M. P. Halsall, A. C. Ferrari, D. W. Boukhvalov, M. I. Katsnelson, A. K. Geim and K. S. Novoselov, Control of Graphene's Properties by Reversible Hydrogenation: Evidence for Graphane. *Science* **2009,** 323, (5914), 610-613.
(24) J. C. Charlier, X. Gonze and J. P. Michenaud, First-Principles Study of Graphite Monofluoride $(CF)_n$. *Phys. Rev. B* **1993,** 47, (24), 16162-16168.
(25) F. Karlický and M. Otyepka, Band Gaps and Optical Spectra of Chlorographene, Fluorographene and Graphane from $G0W_0$, GW_0 and GW Calculations on Top of PBE and HSE06 Orbitals. *J. Chem. Theory Comput.* **2013,** 9, (9), 4155-4164.
(26) H. Sahin, S. Cahangirov, M. Topsakal, E. Bekaroglu, E. Aktrk, R. T. Senger and S. Ciraci, Monolayer Honeycomb Structures of Group IV Elements and III-V Binary Compounds: First-Principles Calculations. *Phys. Rev. B* **2009,** 80, (15), 155453.
(27) Z. Deng, Z. Li and W. Wang, Electron Affinity and Ionization Potential of Two-Dimensional Honeycomb Sheets: A First Principle Study. *Chem. Phys. Lett.* **2015,** 637, 26-31.
(28) X. Gao, Y. Shen, Y. Ma, S. Wu and Z. Zhou, Efficient Band Gap Engineering and Enhanced Optical Absorption of Vertical Germanene/*h*-AlN Bilayer Heterostructure: Potential New Electronics and Optoelectronics. *Phys. Status Solidi B* **2019,** 256, (8), 1800759.
(29) M. A. Khan, J. N. Kuznia, D. T. Olson, T. George and W. T. Pike, GaN/AlN Digital Alloy Short‐period Superlattices by Switched Atomic Layer Metalorganic Chemical Vapor Deposition. *Appl. Phys. Lett.* **1993,** 63, (25), 3470-3472.
(30) E. Bekaroglu, M. Topsakal, S. Cahangirov and S. Ciraci, First-Principles Study of Defects and Adatoms in Silicon Carbide Honeycomb Structures. *Phys. Rev. B* **2010,** 81, (7), 075433.
(31) C.-W. Wu, J.-H. Huang and D.-X. Yao, Tunable Room-Temperature Ferromagnetism in the SiC Monolayer. *J. Magn. Magn. Mater.* **2019,** 469, 306-314.
(32) S. S. Lin, Light-Emitting Two-Dimensional Ultrathin Silicon Carbide. *J. Phys. Chem. C* **2012,** 116, (6), 3951-3955.
(33) L. B. Drissi and F. Z. Ramadan, Excitonic Effects in GeC Hybrid: Many-Body Green's Function Calculations. *Physica E Low Dimens. Syst. Nanostruct.* **2015,** 74, 377-381.
(34) A. Onen, D. Kecik, E. Durgun and S. Ciraci, GaN: From Three- to Two-Dimensional Single-Layer Crystal and its Multilayer Van Der Waals Solids. *Phys. Rev. B* **2016,** 93, (8), 085431.
(35) Z. Qin, G. Qin, X. Zuo, Z. Xiong and M. Hu, Orbitally Driven Low Thermal Conductivity of Monolayer Gallium Nitride (GaN) with Planar Honeycomb Structure: a Comparative Study. *Nanoscale* **2017,** 9, (12), 4295-4309.

(36) C. Ataca, H. Şahin and S. Ciraci, Stable, Single-Layer MX_2 Transition-Metal Oxides and Dichalcogenides in a Honeycomb-Like Structure. *J. Phys. Chem. C* **2012,** 116, (16), 8983-8999.
(37) Y. Ding, Y. Wang, J. Ni, L. Shi, S. Shi and W. Tang, First Principles Study of Structural, Vibrational and Electronic Properties of Graphene-Like MX_2 (M=Mo, Nb, W, Ta; X=S, Se, Te) Monolayers. *Physica B Condens. Matter* **2011,** 406, (11), 2254-2260.
(38) D. S. Koda, F. Bechstedt, M. Marques and L. K. Teles, Coincidence Lattices of 2D Crystals: Heterostructure Predictions and Applications. *J. Phys. Chem. C* **2016,** 120, (20), 10895-10908.
(39) Z. Ma, Z. Hu, X. Zhao, Q. Tang, D. Wu, Z. Zhou and L. Zhang, Tunable Band Structures of Heterostructured Bilayers with Transition-Metal Dichalcogenide and MXene Monolayer. *J. Phys. Chem. C* **2014,** 118, (10), 5593-5599.
(40) R.-N. Wang, X.-R. Zhang, S.-F. Wang, G.-S. Fu and J.-L. Wang, Flatbands in 2D Boroxine-Linked Covalent Organic Frameworks. *Phys. Chem. Chem. Phys.* **2016,** 18, (2), 1258-1264.
(41) A. P. Côté, A. I. Benin, N. W. Ockwig, M. O'Keeffe, A. J. Matzger and O. M. Yaghi, Porous, Crystalline, Covalent Organic Frameworks. *Science* **2005,** 310, (5751), 1166-1170.
(42) Y. Zhou, Z. Wang, P. Yang, X. Zu and F. Gao, Electronic and Optical Properties of Two-Dimensional Covalent Organic Frameworks. *J. Mater. Chem.* **2012,** 22, (33), 16964-16970.
(43) J. Sun, R. Zhang, X. Li and J. Yang, A Many-Body GW + BSE Investigation of Electronic and Optical Properties of C_2N. *Appl. Phys. Lett.* **2016,** 109, (13), 133108.
(44) J. Zhao, J. Zhao, F. Li and Z. Chen, Copper Dimer Supported on a C_2N Layer as an Efficient Electrocatalyst for CO_2 Reduction Reaction: A Computational Study. *J. Phys. Chem. C* **2018,** 122, (34), 19712-19721.
(45) J. Mahmood, E. K. Lee, M. Jung, D. Shin, I.-Y. Jeon, S.-M. Jung, H.-J. Choi, J.-M. Seo, S.-Y. Bae, S.-D. Sohn, N. Park, J. H. Oh, H.-J. Shin and J.-B. Baek, Nitrogenated Holey Two-Dimensional Structures. *Nat. Commun.* **2015,** 6, (1), 6486.
(46) M. R. Ashwin Kishore, A. O. Sjåstad and P. Ravindran, Influence of Hydrogen and Halogen Adsorption on the Photocatalytic Water Splitting Activity of C_2N Monolayer: A First-principles Study. *Carbon* **2019,** 141, 50-58.
(47) S. Guan, Y. Cheng, C. Liu, J. Han, Y. Lu, S. A. Yang and Y. Yao, Effects of Strain on Electronic and Optic Properties of Holey Two-Dimensional C_2N Crystals. *Appl. Phys. Lett.* **2015,** 107, (23), 231904.
(48) J. Xu, J. Mahmood, Y. Dou, S. Dou, F. Li, L. Dai and J.-B. Baek, 2D Frameworks of C_2N and C_3N as New Anode Materials for Lithium-Ion Batteries. *Adv. Mater.* **2017,** 29, (34), 1702007.
(49) X. Ma, Y. Lv, J. Xu, Y. Liu, R. Zhang and Y. Zhu, A Strategy of Enhancing the Photoactivity of g-C_3N_4 via Doping of Nonmetal Elements: A First-Principles Study. *J. Phys. Chem. C* **2012,** 116, (44), 23485-23493.
(50) L.-W. Ruan, Y.-J. Zhu, L.-G. Qiu, Y.-P. Yuan and Y.-X. Lu, First Principles Calculations of the Pressure Affection to *g*-C_3N_4. *Comput. Mater. Sci.* **2014,** 91, 258-265.
(51) S. Lu, C. Li, H. H. Li, Y. F. Zhao, Y. Y. Gong, L. Y. Niu, X. J. Liu and T. Wang, The Effects of Nonmetal Dopants on the Electronic, Optical and Chemical Performances of Monolayer g–C_3N_4 by First-Principles Study. *Appl. Surf. Sci.* **2017,** 392, 966-974.
(52) Y. Xu and S.-P. Gao, Band Gap of C_3N_4 in the GW Approximation. *Int. J. Hydrog. Energy* **2012,** 37, (15), 11072-11080.
(53) X. Zhang, M. Zhao, A. Wang, X. Wang and A. Du, Spin-Polarization and Ferromagnetism of Graphitic Carbon Nitride Materials. *J. Mater. Chem. C* **2013,** 1, (39), 6265-6270.
(54) X. Wang, Y. Zheng, Y. Xu, J. Ben, S. Gao, X. Zhu, Y. Zhuang, S. Yue, H. Bai, Y. Chen, L. Jiang, Y. Ji, Y. Xu, L. Fan, J. Sha, Z. He and Q. Chen, A Novel Peptide Binding to the Cytoplasmic Domain of Class A

Scavenger Receptor Reduces Lipid Uptake in THP-1 Macrophages. *Biochim. Biophys. Acta Mol. Cell Biol. Lipids* **2009,** 1791, (1), 76-83.
(55) B. Yue, Q. Li, H. Iwai, T. Kako and J. Ye, Hydrogen Production using Zinc-Doped Carbon Nitride Catalyst Irradiated with Visible Light. *Sci Technol Adv Mater* **2011,** 12, (3), 034401.
(56) M. A. McGuire, J. Yan, P. Lampen-Kelley, A. F. May, V. R. Cooper, L. Lindsay, A. Puretzky, L. Liang, S. Kc, E. Cakmak, S. Calder and B. C. Sales, High-Temperature Magnetostructural Transition in Van Der Waals-Layered α-$MoCl_3$. *Phys. Rev. Mater.* **2017,** 1, (6), 064001.
(57) Y. Zhang, J. Yun, K. Wang, X. Chen, Z. Yang, Z. Zhang, J. Yan and W. Zhao, First-Principle Study of Graphyne-Like BN Sheet: Electronic Structure and Optical Properties. *Comput. Mater. Sci.* **2017,** 136, 12-19.
(58) V. O. Özçelik and S. Ciraci, Size Dependence in the Stabilities and Electronic Properties of α-Graphyne and Its Boron Nitride Analogue. *J. Phys. Chem. C* **2013,** 117, (5), 2175-2182.
(59) Z. Yang, Y. Zhang, M. Guo and J. Yun, Adsorption of Hydrogen and Oxygen on Graphdiyne and its BN analog Sheets: A Density Functional Theory Study. *Comput. Mater. Sci.* **2019,** 160, 197-206.
(60) M. Long, L. Tang, D. Wang, Y. Li and Z. Shuai, Electronic Structure and Carrier Mobility in Graphdiyne Sheet and Nanoribbons: Theoretical Predictions. *ACS Nano* **2011,** 5, (4), 2593-2600.
(61) H. Bu, M. Zhao, H. Zhang, X. Wang, Y. Xi and Z. Wang, Isoelectronic Doping of Graphdiyne with Boron and Nitrogen: Stable Configurations and Band Gap Modification. *J. Phys. Chem. A* **2012,** 116, (15), 3934-3939.
(62) B. Jang, J. Koo, M. Park, H. Lee, J. Nam, Y. Kwon and H. Lee, Graphdiyne as a High-Capacity Lithium Ion Battery Anode Material. *Appl. Phys. Lett.* **2013,** 103, (26), 263904.
(63) G. Luo, X. Qian, H. Liu, R. Qin, J. Zhou, L. Li, Z. Gao, E. Wang, W.-N. Mei, J. Lu, Y. Li and S. Nagase, Quasiparticle Energies and Excitonic Effects of the Two-Dimensional Carbon Allotrope Graphdiyne: Theory and Experiment. *Phys. Rev. B* **2011,** 84, (7), 075439.
(64) Q. Yue, S. Chang, J. Kang, S. Qin and J. Li, Mechanical and Electronic Properties of Graphyne and Its Family under Elastic Strain: Theoretical Predictions. *J. Phys. Chem. C* **2013,** 117, (28), 14804-14811.
(65) A. L. Ivanovskii, Graphynes and Graphdyines. *Prog. Solid. State Ch.* **2013,** 41, (1), 1-19.
(66) J. A. Marsden and M. M. Haley, Carbon Networks Based on Dehydrobenzoannulenes. 5. Extension of Two-Dimensional Conjugation in Graphdiyne Nanoarchitectures. *J. Org. Chem.* **2005,** 70, (25), 10213-10226.
(67) N. Narita, S. Nagai, S. Suzuki and K. Nakao, Optimized Geometries and Electronic Structures of Graphyne and its Family. *Phys. Rev. B* **1998,** 58, (16), 11009-11014.
(68) J. Kang, J. Li, F. Wu, S.-S. Li and J.-B. Xia, Elastic, Electronic, and Optical Properties of Two-Dimensional Graphyne Sheet. *J. Phys. Chem. C* **2011,** 115, (42), 20466-20470.
(69) X.-M. Wang and S.-S. Lu, Thermoelectric Transport in Graphyne Nanotubes. *J. Phys. Chem. C* **2013,** 117, (38), 19740-19745.
(70) Q. Li, Y. Li, Y. Chen, L. Wu, C. Yang and X. Cui, Synthesis of γ-Graphyne by Mechanochemistry and its Electronic Structure. *Carbon* **2018,** 136, 248-254.
(71) Q. Peng, A. K. Dearden, J. Crean, L. Han, S. Liu, X. Wen and S. De, New Materials Graphyne, Graphdiyne, Graphone, and Graphane: Review of Properties, Synthesis, and Application in Nanotechnology. *Nanotechnol. Sci. Appl.* **2014,** 7, 1-29.
(72) H. Tian, Z. W. Seh, K. Yan, Z. Fu, P. Tang, Y. Lu, R. Zhang, D. Legut, Y. Cui and Q. Zhang, Theoretical Investigation of 2D Layered Materials as Protective Films for Lithium and Sodium Metal Anodes. *Adv. Energy Mater.* **2017,** 7, (13), 1602528.